

A moderate spin for the black hole in X-ray binary MAXI J1348-630 revealed by Insight-HXMT

Hanji Wu,^{1,2} Wei Wang,^{1,2}★ Na Sai,^{1,2} Haifan Zhu,^{1,2} and Jiashi Chen^{1,2}

¹Department of Astronomy, School of Physics and Technology, Wuhan University, Wuhan 430072, China

²WHU-NAOC Joint Center for Astronomy, Wuhan University, Wuhan 430072, China

Accepted XXX. Received YYY; in original form ZZZ

ABSTRACT

MAXI J1348-630 is a low-mass X-ray black hole binary located in the Galaxy and undergone the X-ray outburst in 2019. We analyzed the observation data in very soft state during the outburst between MJD 58588 and MJD 58596 based on the Insight-HXMT observations from 2 – 20 keV via the continuum fitting method to measure the spin of the stellar-mass black hole in MAXI J1348-630. The inner disk temperature and the apparent inner disk radius were found to be 0.47 ± 0.01 keV and $5.33 \pm 0.10 R_g$ from the observation data modeled by the multicolor disc blackbody model. Assuming the distance of the source $D \sim 3.4$ kpc, the mass of the black hole $M \sim 11 M_\odot$, and the inclination of the system $i \sim 29.2^\circ$, the spin is determined to be $a_\star = 0.41 \pm 0.03$ for fixing hardening factor at 1.6 and $n_H = 8.6 \times 10^{21} \text{ cm}^{-2}$. Besides, considering the uncertainty of the parameters D, M, i of this system, with the Monte Carlo analysis, we still confirm the moderate spin of the black hole as $a_\star = 0.42^{+0.13}_{-0.50}$. Some spectral parameters (e.g., column density and hardening factor) which could affect the measurements of the BH spin are also briefly discussed.

Key words: X-rays: binaries – accretion discs – X-rays : individual (MAXI J1348-630)

1 INTRODUCTION

The black hole (BH) spin will reveal their formation and evolution and affect fruitful astrophysical phenomena. The spin would be helpful for understanding the relativistic jets launched by Blandford–Znajek (BZ) mechanism (Blandford & Znajek 1977) or Blandford–Payne (BP) mechanism (Blandford & Payne 1982), and the ratio between the energy of accretion matter and electromagnetic radiation could vary by almost one order of magnitude, which depends on how rapidly the black hole rotates (Bardeen et al. 1972). For exploring the black hole spin a , the dimensionless spin parameter a_\star is used to characterize the spin in different mass black holes, defined as $a_\star \equiv \frac{a}{M} = \frac{cJ}{GM^2}$ (Kerr 1963; Misner et al. 1973), where the M and J represent the mass and the angular momentum of the black hole, the c for light speed, G for gravitational constant. In an accreting black hole, the spin a_\star will shape the temperature of the inner disk (Zhang et al. 1997; McClintock et al. 2013), due to the spin-dependent innermost stable circular orbit (ISCO) (Bardeen et al. 1972), so that the more binding energy from the accreting matter heats the inner disk reaching a higher temperature. In an accreting black hole X-ray binary (Remillard & McClintock 2006), the outburst usually obeys the "Q"-shape feature evolving from the low hard state (LHS) though the intermediate state (IS) to the high soft state (HSS), then back to LHS. The theoretical simulations (Shafee et al. 2008; Penna et al. 2010) suggest that the inner disc radius (R_{in}) would extend to the ISCO in the high soft state, the inner disc radius R_{in} would not change (Steiner et al. 2010; Kulkarni et al. 2011).

At present, there are two main methods to measure the BH spin, namely the Fe K α emission line method which reflects the characteristic of reflected fluorescence in the disk (Fabian et al. 1989; Dabrowski et al. 1997; Reynolds & Nowak 2003), and the continuum-fitting (CF) model based on the Novikov–Thorne thin disc model (Novikov & Thorne 1973; Zhang et al. 1997; Li et al. 2005). The basic assumption of the CF method is the accretion disc extending into the innermost stable circular orbit (ISCO), and in order to derive a credible spin by the CF method, the luminosity must also be limited to below 30% of the Eddington limit to ensure the application approximation of thin disk assumption. The CF method has measured the spin of many stellar-mass BHs (Guan et al. 2021; Zhao et al. 2021; Shafee et al. 2005; Steiner et al. 2011; McClintock et al. 2006; Zhao et al. 2020). In this paper, we will use the CF method to constrain the black hole spin of MAXI J1348-630.

The Gas Slit Camera (GSC) onboard Monitor of All-sky X-ray Image discovered MAXI J1348-630 on Jan 26 2019 (Matsuoka et al. 2009; Yatabe et al. 2019), which is classified as a black hole X-ray binary (BHXR) through the mass estimate, light curve evolution and spectral features (Tominaga et al. 2020; Belloni et al. 2020; Carotenuto et al. 2019; Denisenko et al. 2019; Jana et al. 2019; Kennea & Negoro 2019; Russell et al. 2019; Sanna et al. 2019; Yatabe et al. 2019). The MAXI J1348-630 obeyed the "Q"-shape feature during the 2019 outbursts in the Swift/XRT (Tominaga et al. 2020) data and the NICER data (Zhang et al. 2020b). A giant dust scattering ring around this source is discovered in SRG/eROSITA data, and with the joint data from XMM-Newton, MAXI, and Gaia, Lamer et al. (2021) estimated the distance of MAXI J1348-630 at 3.39 ± 0.34 kpc and the black hole mass of $11 \pm 2 M_\odot$. From the

★ E-mail: wangwei2017@whu.edu.cn

spectral evolution during the 2019 outburst using the Swift and MAXI detectors, the two-component advective flow model estimated the black hole mass to be $9.1^{+1.6}_{-1.2} M_{\odot}$ (Jana et al. 2020). The Australian Square Kilometre Array Pathfinder (ASKAP) and MeerKAT also provided the observation of MAXI J1348-630 and showed that the H I absorption spectra of this source suggested the distance as $2.2^{+0.5}_{-0.6}$ kpc (Chauhan et al. 2021) and Carotenuto et al. (2022a) modeled the physical properties of jets from MAXI J1348-630.

The inclination angle of the binary system is also an important parameter for black hole research. Carotenuto et al. (2022a) obtained the inclination of 29 ± 3 degrees by modelling the jet from the radio data and Carotenuto et al. (2022b) gave a upper limit of the inclination 46° by the radio image. The spectral analysis of the reflection component in the X-ray spectrum determined the inclination of $\sim 29^{\circ} - 40^{\circ}$ (Mall et al. 2022; Kumar et al. 2022; Jia et al. 2022; Wu et al. 2023), which is well consistent with the jet results. The analysis of the reflection component during the second outburst in 2019 also found a inclination of $30^{\circ} - 46^{\circ}$ (Bhowmick et al. 2022). Liu et al. (2022) suggested the inclination of $\sim 30^{\circ}$ based on studying quasi-periodic oscillations (QPO). Titarchuk & Seifina (2022) used the scaling technique through the correlation between photon index and normalization proportional to mass accretion rate and gave the inclination of 65 ± 7 degrees, which deviates far from other independent results, maybe due to the large uncertainties of the correlation.

Furthermore, both type-B and type-C QPO were found in this BHXRB (Alabarta et al. 2022; Belloni et al. 2020; Liu et al. 2022). The timing analysis illustrated that there is a time lag in the 0.5-80 keV energy band (Jithesh et al. 2021) which revealed the time lag between the disk component and the corona radiation has been discovered (Weng et al. 2021). In the infrared and optical bands, the absorption lines of H, He which point to disc wind signatures have been founded (Panizo-Espinar et al. 2022). In hard state, the Fe absorption line with high blue-shift is also found in NuSTAR data, suggesting that there are ultra-fast outflows (Chakraborty et al. 2021; Wu et al. 2023) and from the Insight-HXMT data and Swift data, Zhang et al. (2022) found the evidence of the optically thin disc feature. To figure out the physical properties of the disc, the reflection component is fitted by Chakraborty et al. (2021) which showed that the density of the disc is over 10^{20}cm^{-3} . In quiescence, Carotenuto et al. (2022b) illustrated that this source belongs to the standard (radio-loud) track.

Based on the long-term observation from Insight-HXMT in wide-band X-rays, we constrain the spin of the black hole in MAXI J1348-630 by the CF method. This paper is organized as follows: the observation and data reduction in section 2, data analysis and CF method modeling results in section 3, conclusion and discussion in section 4.

2 OBSERVATIONS AND DATA REDUCTION

The Insight-HXMT launched on Jun 15 2017, which is the first hard X-ray observatory of China (Zhang et al. 2020a), observed MAXI J1348-630 for over 50 days from Jan 27 2019 to Jul 29 2019. The Insight-HXMT consists of a Low Energy (LE) telescope of which the effective area is 384cm^2 in the energy range from 1 keV to 15 keV (Chen et al. 2020), a Medium Energy (ME) telescope of which the effective area is 952cm^2 in the energy range from 5 keV to 30 keV (Cao et al. 2020), and the High Energy X-ray telescope (HE; 20-250 keV) with the effective area of 5100cm^2 (Liu et al. 2020). The pileup effects of Insight-HXMT LE telescope are extremely low ($<1\%$ @ 18000cts/s , see Chen et al. 2020). The HE Net count rate

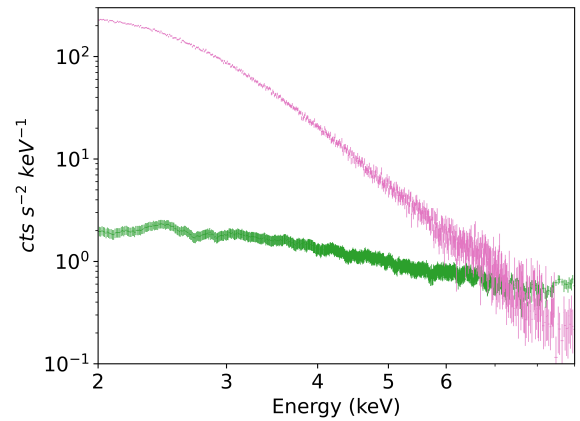


Figure 1. This figure shows the background count rate (green dots) and the source spectrum count rate (purple dots) from ObsID 301 for the LE telescope.

from the source was lower than the background in the soft state during our observations, thus we will only use the LE and ME data for the analysis in this work.

We extract the spectra from Insight-HXMT Data using the Insight-HXMT Data Analysis software (HXMTDAS) v2.04¹. We jointly analyze two telescopes (LE, ME) by combining the 2 keV to 9 keV from LE due to high background noises leading to low Net count rate above 9 keV and the instrumental feature below 2 keV (Li et al. 2023), and the 10 keV to 20 keV from ME due to the calibration uncertainties from 21 – 24 keV and the background noises leading to low Net count rate above ~ 20 keV for the soft state (Cao et al. 2020), and inserting two cross-normalization constants (the constant model in XSPEC), besides, we freeze the LE constant and let the ME constant vary freely. Using the recommended criteria: the elevation angle > 10 degrees, the geomagnetic cutoff rigidity > 8 GeV, at least 300 s away from the South Atlantic Anomaly (SAA) and the pointing offset angle $< 0.1^{\circ}$. We generate the background files by LEBKGMAP and MEBKGMAP to estimate the background count rates (Liao et al. 2020). The background count rates are relatively stable and the source spectrum count rates decrease with energy (as the example for the LE telescope shown in Fig. 1), in the soft state of this BH system, background magnitude would be much lower than the source count rate below 8 keV, and at the similar levels of the source spectrum above ~ 8 keV by LE telescope and in the band of 10 – 20 keV by ME telescope. The LE detector’s readout time is around 1 ms without dead time. The ME detector dead time effect in the band of 10–20 keV is about 1% is calculated by Zhang et al. (2022), which is within our statistical uncertainty.

3 DATA ANALYSIS

We investigate the X-ray spectra by the XSPEC v12.12.1². In all following models, the galactic neutral hydrogen column density is fixed at $8.6 \times 10^{21} \text{cm}^{-2}$ in TBabs composition (Tominaga et al. 2020). We insert a cross-normalization constant between LE and ME and we freeze the constant in LE as standard as well as the constant of ME can vary freely. The confidence level of every parameter is set to 90% to produce the error range. We analyze the spectra of the observational data illustrated in Fig. 2 as red crosses.

¹ <http://hxmtweb.ihep.ac.cn/software.jhtml>

² <https://heasarc.gsfc.nasa.gov/xanadu/xspec/>

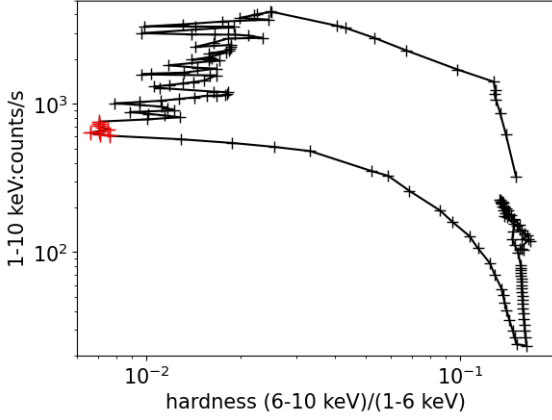


Figure 2. The HID of MAXI J1348-630 during the 2019 outburst observed by Insight-HXMT; The hardness (the count rate ratio between 6-10 keV and 1-6 keV) versus the total count rate by LE.

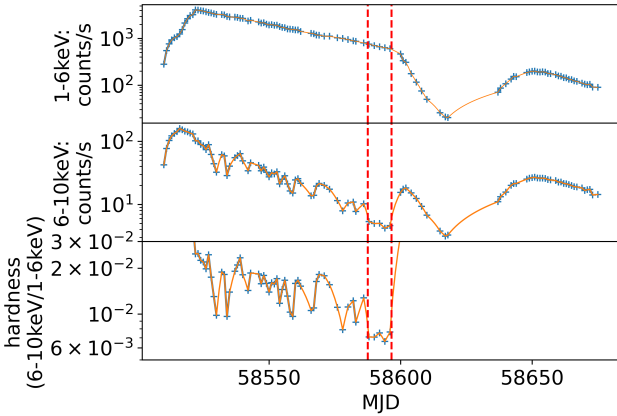


Figure 3. The light curves of MAXI J1348-630 in units of count rates observed by Insight-HXMT. The top panel illustrates the light curve of 1-6 keV photons, the middle panel for the light curve of 6-10 keV, and the bottom panel for the hardness which is the ratio between the light curve of 6-10 keV and 1-6 keV. We investigate the observational data between the red lines (MJD from 58588 to 58596).

3.1 Hardness intensity diagram (HID)

In this outburst, the Insight-HXMT provides the pointing observations from MJD 58510 to MJD 58693, and the LE intensity versus hardness defined as the count rate between 6-10 keV and 1-6 keV are presented in hardness-intensity diagram Fig. 2, which follows a "q" pattern. After the peak count rate at MJD 58523, The 6-10 keV photon count rates oscillate until MJD 58588, which is illustrated in Fig. 3. And the hardness ratio evolved from 0.02 to $\sim 8 \times 10^{-3}$, between MJD 58588 and 58596, the hardness reached the lowest value around $\sim 6 \times 10^{-3}$. After the softest state, the 1-6 keV photon count rate decreased by two orders of magnitude steeply and the 6-10 keV photon count rate increased by several times, and the BH system transited to the hard state again and finished the main outburst. In the following spectral analysis, we will investigate the observational data from MJD 58588 to MJD 58596. There are 11 times of observations in this period, which are illustrated in Table 1.

3.2 The spectral fittings: continuum

We will analyze the spectral properties of Insight-HXMT observations in the softest state from MJD 58588 to 58596 when the hardness is about 6×10^{-3} , which is illustrated between the red dash lines in Fig. 3. The four models we used including phenomenological and physical models to characterize the broad-band spectra (2-9 keV from LE telescope and 10-20 keV from ME telescope) will be introduced in the following four subsections. The model *Tbabs* is included by all models, which considers the interstellar absorption effect with Wilms et al. (2000) abundances and Verner et al. (1996) cross-section and the column density (N_H) is fixed at the well studied value (Tominaga et al. 2020) $8.6 \times 10^{21} \text{ cm}^{-2}$ which is also used in previous work (Zdziarski et al. 2022; Cangemi et al. 2022; Carotenuto et al. 2022a; Jia et al. 2022; Chakraborty et al. 2021; Saha et al. 2021), due to the below 2 keV photons ignored leading to insufficient constraints on the column density (N_H).

In the continuum fitting method the parameters like the BH mass, source distance and the inclination of the system are important and affect the results. Thus, based on the previous independent measurements, the BH mass of $M_{BH} = 11 \pm 2 M_\odot$, the distance of $D = 3.39 \pm 0.34 \text{ kpc}$ (Lamer et al. 2021), and the inclination of $i = 29.2^{+0.3}_{-0.5}$ degrees (Jia et al. 2022) as fiducial values are adopted in the following spectral fittings. The inclination $i = 29.2^{+0.3}_{-0.5}$ degrees used here is also consistent with the values by several independent methods including reflection model, jet model from radio data, and QPO research (Mall et al. 2022; Kumar et al. 2022; Jia et al. 2022; Carotenuto et al. 2022a; Liu et al. 2022). At the fiducial values, the flux (2-20 keV) is $\sim (1-2) \times 10^{-8} \text{ erg s}^{-1} \text{ cm}^{-2}$, and X-ray luminosity of this source is $\sim (2-4) \times 10^{37} \text{ erg s}^{-1}$ during the softest state at a distance of 3.4 kpc. If taking the BH mass at $11 M_\odot$, the Eddington luminosity will be $1.4 \times 10^{39} \text{ erg s}^{-1}$, then this source during the period has an accretion luminosity less than 3% of Eddington luminosity. Furthermore, we also noticed that the mass, distance, and inclination of the black hole in MAXI J1348-630 are pretty uncertain, so in section 3.3, we discuss the influence of these three key parameters (the mass, distance, and inclination of the black hole in MAXI J1348-630) on the spin determination.

3.2.1 Model 1: *constant * Tbabs * (diskbb + powerlaw)*

Firstly, the spectrum is fitted by the multicolor disc blackbody model *diskbb* (Mitsuda et al. 1984; Makishima et al. 1986) and a power-law component: *constant * Tbabs * (diskbb + powerlaw)*. The results of all fitted parameters in model 1 are shown in Table 2 and Fig. 4, and the example of spectra and residuals are shown in Fig. 5. The inner disc temperature is determined at around 0.47 keV, and $\Gamma_{powerlaw} \sim 3.04$. The parameter N_{diskbb} of *diskbb* is related to the apparent inner disc radius by the function: $N_{diskbb} = (\frac{R_{in}}{D_{10}})^2 \cos i$, where the R_{in} is the apparent inner disc radius, D_{10} for the distance in units of 10 kpc, i for the inclination of the system (Kubota et al. 1998), thus, the apparent inner disc radius R_{in} is around $5.3 R_g$.

3.2.2 Model 2: *constant * Tbabs * (kerrbb + powerlaw)*

Then, we take the *kerrbb* model (Li et al. 2005) to replace the *diskbb* component to determine the black hole's spin a_* . We fix the hardening factor at 1.6 (Shimura & Takahara 1995; Shafee et al. 2005) and use the fiducial values: the BH mass of $M_{BH} = 11 \pm 2 M_\odot$, the distance of $D = 3.39 \pm 0.34 \text{ kpc}$ (Lamer et al. 2021), and the inclination of $i = 29.2^{+0.3}_{-0.5}$ degree (Jia et al. 2022), besides, freeze the normalization of *kerrbb*. The results of all fitted parameters are

Table 1. Insight-HXMT observation details for MAXI J1348-630.

Obs. ID	Obs. date (yyyy-mm-dd)	Obs. date (MJD)	LE Exposure(s)	ME Exposure(s)	Abbreviation
P02140206201	2019-04-15	58588	2933	2542	201
P02140206202	2019-04-15	58588	1556	2305	202
P02140206301	2019-04-17	58590	2933	2808	301
P02140206302	2019-04-17	58590	1855	2333	302
P02140206401	2019-04-19	58592	1731	1948	401
P02140206402	2019-04-20	58593	947	1220	402
P02140206403	2019-04-20	58593	1017	1366	403
P02140206501	2019-04-21	58594	1855	1948	501
P02140206601	2019-04-23	58596	2633	2762	601
P02140206602	2019-04-23	58596	2095	2115	602
P02140206603	2019-04-23	58596	1616	2004	603

Table 2. Spectral fitting results for Model 1: constant * Tbabs * (diskbb + powerlaw)

Obs.(→) component(↓)	parameter(↓)	201	202	301	302	401	402
TBabs	$N_{\text{H}} (\times 10^{22} \text{cm}^{-2})$	0.86^{\dagger}	0.86^{\dagger}	0.86^{\dagger}	0.86^{\dagger}	0.86^{\dagger}	0.86^{\dagger}
powerlaw	Γ_{powerlaw}	2.87 ± 0.11	2.46 ± 0.12	2.77 ± 0.12	2.96 ± 0.14	2.97 ± 0.17	3.67 ± 0.25
	N_{powerlaw}	$2.07^{+0.49}_{-0.39}$	$0.91^{+0.23}_{-0.18}$	$1.51^{+0.37}_{-0.29}$	$2.09^{+0.63}_{-0.48}$	$1.87^{+0.70}_{-0.51}$	$5.82^{+3.29}_{-2.18}$
	$T_{\text{in}} (\text{keV})$	0.49 ± 0.01	0.49 ± 0.01	0.48 ± 0.01	0.48 ± 0.01	0.47 ± 0.01	0.47 ± 0.01
diskbb	N_{diskbb}	$55486.09^{+1107.29}_{-1071.60}$	$53350.49^{+1450.93}_{-1393.49}$	$54676.14^{+1169.21}_{-1128.09}$	$56966.02^{+1522.29}_{-1470.96}$	$57170.00^{+1621.38}_{-1571.52}$	$54230.64^{+2266.31}_{-2522.51}$
	C_{ME}	0.98 ± 0.07	0.87 ± 0.06	0.98 ± 0.07	1.07 ± 0.09	1.03 ± 0.11	$1.67^{+0.26}_{-0.22}$
	χ^2/ν	1130.63/991	1106.90/991	1089.43/991	1265.14/991	1028.30/991	1070.39/991
	χ^2_{ν}	1.14	1.12	1.10	1.28	1.04	1.08
Obs.(→) component(↓)	parameter(↓)	403	501	601	602	603	
TBabs	$N_{\text{H}} (\times 10^{22} \text{cm}^{-2})$	0.86^{\dagger}	0.86^{\dagger}	0.86^{\dagger}	0.86^{\dagger}	0.86^{\dagger}	
powerlaw	Γ_{powerlaw}	3.07 ± 0.22	3.37 ± 0.21	3.25 ± 0.16	2.89 ± 0.18	3.16 ± 0.17	
	N_{powerlaw}	$2.22^{+1.12}_{-0.74}$	$2.93^{+1.37}_{-0.95}$	$2.58^{+0.88}_{-0.66}$	$1.40^{+0.55}_{-0.39}$	$2.22^{+0.80}_{-0.58}$	
	$T_{\text{in}} (\text{keV})$	0.47 ± 0.01	0.47 ± 0.01	0.46 ± 0.01	0.46 ± 0.01	0.46 ± 0.01	
diskbb	N_{diskbb}	$57036.20^{+2117.68}_{-2032.50}$	$57737.78^{+1556.00}_{-1507.49}$	$59552.11^{+1465.69}_{-1420.43}$	$58819.82^{+1926.28}_{-1847.55}$	$59787.99^{+1697.83}_{-1631.34}$	
	C_{ME}	$1.03^{+0.13}_{-0.13}$	$1.19^{+0.15}_{-0.16}$	$1.21^{+0.12}_{-0.13}$	$1.05^{+0.11}_{-0.13}$	$1.30^{+0.13}_{-0.14}$	
	χ^2/ν	943.36/991	995.21/991	1018.32/991	1008.91/991	1024.60/991	
	χ^2_{ν}	0.95	1.00	1.03	1.02	1.03	

shown in Table 3 and Fig. 7. The example of spectral data and residuals are shown in Fig. 6. Thus, we get the spin of the black hole in MAXI J11348-630 $a_{\star} \sim 0.41 \pm 0.03$ in model 2 and the effective mass accretion rate is $0.97 \times 10^{18} \text{g/s}$.

3.2.3 Model 3: constant * Tbabs * (kerrbb + nthcomp)

For investigating the influence of the different powerlaw components on the results of disc components, we replace the powerlaw with the nthcomp (the spectra from Comptonization by the thermal electrons (Zdziarski et al. 1996, 2020; Niedźwiecki et al. 2019)). Due to the energy range which we study can't reach the cutoff energy, we freeze the temperature of electrons at 30 keV (Jia et al. 2022; Chakraborty et al. 2021) which is the electron temperature found by the relxillCp reflection model (García et al. 2015; Dauser et al. 2014), and freeze the seed photon temperature at 0.1 keV. The results of all fitted parameters are shown in Table 4 and Fig. 9. The example of data and residuals are shown in Fig. 8. Thus, we get the spin of the black hole

in MAXI J11348-630 $a_{\star} \sim 0.41 \pm 0.03$ in model 2 and the effective mass accretion rate $\sim 0.97 \times 10^{18} \text{g/s}$.

3.2.4 Model 4: constant * Tbabs * (diskbb + nthcomp)

Finally, we test the multicolor disc blackbody model diskbb with nthcomp component. The nthcomp component is set the same as model 3. The results of all fitted parameters are shown in Table 5 and Fig. 11. The example of data and residuals are shown in Fig. 10. The results of diskbb in model 4 are quite close to model 1 results: the apparent inner disc radius $R_{\text{in}} \sim 5.3R_g$ and the inner disc temperature at around 0.47 keV.

3.3 Uncertainty analysis

In the above fittings, we used the BH mass of $M_{\text{BH}} = 11 \pm 2 M_{\odot}$, the distance of $D = 3.39 \pm 0.34 \text{ kpc}$ (Lamer et al. 2021), and the inclination of $i = 29.2^{+0.3}_{-0.5}$ degrees (Jia et al. 2022) as fiducial values. However, the BH mass, the distance from the source, the inclination

Table 3. Spectral fitting results for Model 2: constant * Tbabs * (kerrbb + powerlaw)

Obs.(→) component(↓)	parameter(↓)	201	202	301	302	401	402
TBabs powerlaw	$N_{\text{H}} (\times 10^{22} \text{cm}^{-2})$	0.86^{\dagger}	0.86^{\dagger}	0.86^{\dagger}	0.86^{\dagger}	0.86^{\dagger}	0.86^{\dagger}
	Γ_{powerlaw}	2.60 ± 0.11	2.27 ± 0.12	2.51 ± 0.12	2.68 ± 0.14	2.66 ± 0.17	3.26 ± 0.27
	N_{powerlaw}	$1.16^{+0.28}_{-0.22}$	$0.60^{+0.15}_{-0.12}$	$0.86^{+0.21}_{-0.17}$	$1.16^{+0.36}_{-0.27}$	$0.98^{+0.39}_{-0.27}$	$2.55^{+1.74}_{-1.02}$
kerrbb	a_{\star}	0.43 ± 0.01	0.45 ± 0.02	0.44 ± 0.01	0.42 ± 0.01	0.42 ± 0.01	0.43 ± 0.02
	$\dot{M} (10^{18} \text{g/s})$	1.04 ± 0.01	1.02 ± 0.02	0.98 ± 0.01	1.00 ± 0.02	0.97 ± 0.02	0.93 ± 0.02
	C_{ME}	$0.89^{+0.06}_{-0.07}$	$0.84^{+0.06}_{-0.07}$	$0.90^{+0.06}_{-0.07}$	$0.98^{+0.08}_{-0.09}$	$0.93^{+0.09}_{-0.11}$	$1.48^{+0.21}_{-0.24}$
	χ^2/ν	1043.83/991	1031.93/991	1000.12/991	1195.61/991	981.7/991	1044.89/991
	χ^2_{ν}	1.05	1.04	1.01	1.21	0.99	1.05
Obs.(→) component(↓)	parameter(↓)	403	501	601	602	603	
TBabs powerlaw	$N_{\text{H}} (\times 10^{22} \text{cm}^{-2})$	0.86^{\dagger}	0.86^{\dagger}	0.86^{\dagger}	0.86^{\dagger}	0.86^{\dagger}	
	Γ_{powerlaw}	$2.77^{+0.23}_{-0.22}$	$3.03^{+0.21}_{-0.26}$	2.96 ± 0.16	2.67 ± 0.17	2.90 ± 0.16	
	N_{powerlaw}	$1.19^{+0.65}_{-0.41}$	$1.46^{+0.58}_{-0.70}$	$1.42^{+0.36}_{-0.49}$	$0.88^{+0.26}_{-0.34}$	$1.30^{+0.46}_{-0.33}$	
kerrbb	a_{\star}	0.41 ± 0.03	0.39 ± 0.02	0.37 ± 0.02	0.38 ± 0.03	0.37 ± 0.02	
	$\dot{M} (10^{18} \text{g/s})$	0.96 ± 0.02	0.96 ± 0.02	0.94 ± 0.02	0.93 ± 0.03	0.94 ± 0.02	
	C_{ME}	$0.93^{+0.14}_{-0.12}$	$1.06^{+0.15}_{-0.14}$	$1.09^{+0.12}_{-0.11}$	$0.98^{+0.12}_{-0.11}$	$1.20^{+0.13}_{-0.12}$	
	χ^2/ν	927.02/991	974.47/991	973.57/991	974.41/991	966.05/991	
	χ^2_{ν}	0.94	0.98	0.98	0.98	0.97	

Table 4. Spectral fitting results for Model 3: constant * Tbabs * (kerrbb + nthcomp)

Obs.(→) component(↓)	parameter(↓)	201	202	301	302	401	402
TBabs nthcomp	$N_{\text{H}} (\times 10^{22} \text{cm}^{-2})$	0.86^{\dagger}	0.86^{\dagger}	0.86^{\dagger}	0.86^{\dagger}	0.86^{\dagger}	0.86^{\dagger}
	Γ_{nthcomp}	2.47 ± 0.10	2.18 ± 0.10	2.39 ± 0.10	$2.53^{+0.13}_{-0.12}$	$2.53^{+0.15}_{-0.15}$	$3.06^{+0.25}_{-0.27}$
	N_{nthcomp}	$0.95^{+0.17}_{-0.21}$	$0.51^{+0.09}_{-0.11}$	$0.71^{+0.16}_{-0.13}$	$0.91^{+0.26}_{-0.20}$	$0.79^{+0.25}_{-0.21}$	$1.86^{+1.26}_{-0.71}$
kerrbb	a_{\star}	0.44 ± 0.01	0.46 ± 0.02	0.44 ± 0.01	0.42 ± 0.01	0.42 ± 0.01	0.43 ± 0.02
	$\dot{M} (10^{18} \text{g/s})$	1.04 ± 0.01	1.02 ± 0.02	0.98 ± 0.01	1.00 ± 0.02	0.97 ± 0.02	0.94 ± 0.02
	C_{ME}	0.87 ± 0.06	0.82 ± 0.06	$0.88^{+0.07}_{-0.06}$	$0.96^{+0.09}_{-0.08}$	$0.91^{+0.10}_{-0.09}$	$1.44^{+0.24}_{-0.20}$
	χ^2/ν	1065.73/991	1043.14/991	1016.76/991	1216.24/991	996.94/991	1055.53/991
	χ^2_{ν}	1.08	1.05	1.03	1.23	1.01	1.07
Obs.(→) component(↓)	parameter(↓)	403	501	601	602	603	
TBabs nthcomp	$N_{\text{H}} (\times 10^{22} \text{cm}^{-2})$	0.86^{\dagger}	0.86^{\dagger}	0.86^{\dagger}	0.86^{\dagger}	0.86^{\dagger}	
	Γ_{nthcomp}	$2.62^{+0.20}_{-0.21}$	$2.84^{+0.21}_{-0.24}$	$2.82^{+0.14}_{-0.15}$	$2.55^{+0.19}_{-0.16}$	$2.75^{+0.14}_{-0.15}$	
	N_{nthcomp}	$0.95^{+0.48}_{-0.31}$	$1.07^{+0.64}_{-0.36}$	$1.14^{+0.37}_{-0.27}$	$0.73^{+0.26}_{-0.23}$	$1.04^{+0.34}_{-0.25}$	
kerrbb	a_{\star}	0.42 ± 0.02	$0.40^{+0.01}_{-0.03}$	0.37 ± 0.02	0.39 ± 0.03	0.37 ± 0.02	
	$\dot{M} (10^{18} \text{g/s})$	0.96 ± 0.02	0.95 ± 0.03	0.94 ± 0.02	0.93 ± 0.03	0.94 ± 0.02	
	C_{ME}	$0.90^{+0.14}_{-0.12}$	$1.03^{+0.13}_{-0.16}$	$1.07^{+0.12}_{-0.10}$	$0.97^{+0.12}_{-0.10}$	$1.17^{+0.13}_{-0.11}$	
	χ^2/ν	926.16/991	980.22/991	989.21/991	993.09/991	997.22/991	
	χ^2_{ν}	0.93	0.99	1.00	1.00	1.01	

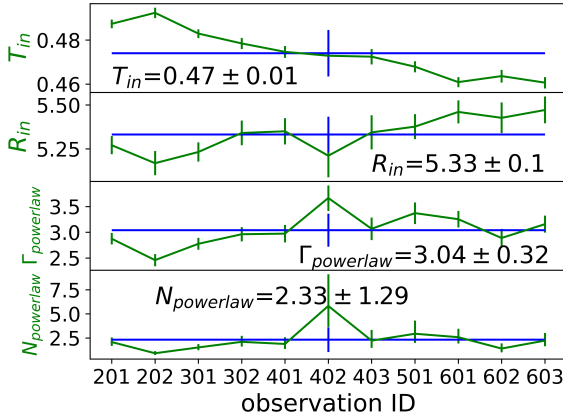
for this source are still quite uncertain. The minimum estimated black hole mass is about $8 M_{\odot}$ (Jana et al. 2020), the maximum one of $13 M_{\odot}$ (Lamer et al. 2021); the distance to the source could be from about 2.2 kpc (Chauhan et al. 2021) to about 4 kpc (Lamer et al. 2021). The inclination angle of the binary has been estimated as the range of $\sim 25^{\circ} - 46^{\circ}$ (Jia et al. 2022; Carotenuto et al. 2022b; Bhowmick et al. 2022; Wu et al. 2023), based on the independent measurements. Titarchuk & Seifina (2022) suggested a large inclination using a correlation technique, however this marginal correlation and scaling method will induce a large uncertainty, so that in the following we still

choose the inclination range between $25^{\circ} - 46^{\circ}$. With the different parameter spaces, the values of X-ray luminosity and Eddington luminosity can be calculated, the accretion luminosity of the BH system is generally below 6% of Eddington luminosity.

Finally, following the similar Monte Carlo method by Guan et al. (2021); Zhao et al. (2021), we set over 2000 sets of parameters: the inclination from 25° to 46° , the black hole mass from $8 M_{\odot}$ to $13 M_{\odot}$, the distance from 1.6 kpc to 4 kpc, evenly distributed to test the influence by different parameters, then, we use the model 2 to figure out the distribution of the a_{\star} . The final distribution of

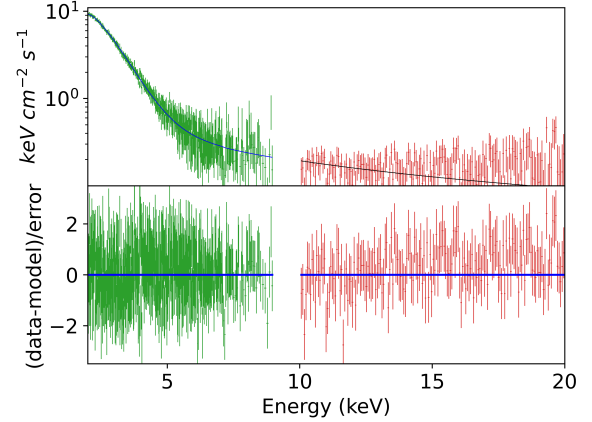
Table 5. Spectral fitting results for Model 4: constant * Tbars * (diskbb + nthcomp)

Obs.(→) component(↓)	parameter(↓)	201	202	301	302	401	402
TBabs	$N_{\text{H}} (\times 10^{22} \text{cm}^{-2})$	0.86^{\dagger}	0.86^{\dagger}	0.86^{\dagger}	0.86^{\dagger}	0.86^{\dagger}	0.86^{\dagger}
nthcomp	Γ_{nthcomp}	2.73 ± 0.10	2.33 ± 0.10	2.63 ± 0.11	2.79 ± 0.13	2.82 ± 0.16	3.47 ± 0.25
	N_{nthcomp}	$1.65^{+0.37}_{-0.30}$	$0.74^{+0.17}_{-0.14}$	$1.20^{+0.28}_{-0.22}$	$1.60^{+0.46}_{-0.35}$	$1.47^{+0.53}_{-0.38}$	$4.38^{+2.59}_{-1.63}$
diskbb	$T_{\text{in}} (\text{keV})$	0.49 ± 0.01	0.49 ± 0.01	0.48 ± 0.01	0.48 ± 0.01	0.48 ± 0.01	0.47 ± 0.01
	N_{diskbb}	$55348.54^{+1132.25}_{-1098.08}$	$52913.45^{+1429.77}_{-1379.49}$	$54410.04^{+1184.22}_{-1144.24}$	$56729.49^{+1561.19}_{-1498.12}$	$57023.17^{+1668.25}_{-1610.38}$	$55142.53^{+2137.58}_{-2157.72}$
	C_{ME}	$0.96^{+0.07}_{-0.06}$	$0.85^{+0.07}_{-0.06}$	0.95 ± 0.07	$1.04^{+0.09}_{-0.08}$	$1.01^{+0.11}_{-0.10}$	$1.64^{+0.26}_{-0.22}$
	χ^2/ν	1153.01/991	1120.52/991	1109.78/991	1285.89/991	1040.74/991	1081.20/991
	χ^2_{ν}	1.16	1.13	1.12	1.30	1.05	1.09
Obs.(→) component(↓)	parameter(↓)	403	501	601	602	603	
TBabs	$N_{\text{H}} (\times 10^{22} \text{cm}^{-2})$	0.86^{\dagger}	0.86^{\dagger}	0.86^{\dagger}	0.86^{\dagger}	0.86^{\dagger}	
nthcomp	Γ_{nthcomp}	2.91 ± 0.20	3.21 ± 0.20	3.09 ± 0.16	2.75 ± 0.16	2.99 ± 0.16	
	N_{nthcomp}	$1.74^{+0.84}_{-0.56}$	$2.34^{+1.08}_{-0.74}$	$2.03^{+0.68}_{-0.50}$	$1.12^{+0.42}_{-0.30}$	$1.73^{+0.60}_{-0.43}$	
diskbb	$T_{\text{in}} (\text{keV})$	0.47 ± 0.01	0.47 ± 0.01	0.46 ± 0.01	0.46 ± 0.01	0.46 ± 0.01	
	N_{diskbb}	$56986.55^{+2170.17}_{-2100.60}$	$58042.18^{+1575.57}_{-1525.28}$	$59675.14^{+1510.41}_{-1465.52}$	$58593.56^{+1952.74}_{-1878.95}$	$59736.40^{+1752.87}_{-1677.46}$	
	C_{ME}	$1.00^{+0.15}_{-0.13}$	$1.18^{+0.17}_{-0.15}$	$1.19^{+0.13}_{-0.12}$	$1.03^{+0.13}_{-0.10}$	$1.28^{+0.14}_{-0.12}$	
	χ^2/ν	950.50/991	1003.96/991	1033.12/991	1017.55/991	1039.67/991	
	χ^2_{ν}	0.96	1.01	1.04	1.03	1.05	

**Figure 4.** The fitted parameters versus the observation ID with model 1. T_{in} is the inner disc temperature, R_{in} for the apparent inner disc radius in units of R_g , Γ_{powerlaw} for the photon index in powerlaw model, N_{powerlaw} for the normalization of powerlaw model. The average results are shown in black font.

a_{\star} is shown in Fig. 12, which we use the python package fitter (Cokelaer et al. 2022) to fit. The best fitting function is genlogistic (generalized logistic) distribution: $f(x, c) = c \frac{\exp(-x)}{(1+\exp(-x))^{c+1}}$, where $c=0.05$, giving $a_{\star} = 0.42^{+0.13}_{-0.50}$ with 68.3% (1σ error) confidence level.

In the previous spectral fittings, we have fixed the column density N_{H} at a normal value. We also tested the impact of this parameter, when N_{H} is free, on fitting the spin parameter a_{\star} which has been illustrated in Fig. 13. Although the column density N_{H} is hard to restrict, the best-fit results still give $a_{\star} \sim 0.41$ and $N_{\text{H}} \sim 8.6 \times 10^{21} \text{cm}^{-2}$. The former researches (Wang et al. 2022; Zdziarski et al. 2022; Li et al. 2023) have shown that the difference of the absolute flux between Insight-HXMT and NuSTAR is within a few percent, which leads to

**Figure 5.** The spectrum and the residual for ObsID 403 with model 1 as an example. The green and red data points correspond to LE telescope and ME telescope, respectively.

the spin uncertainty $\lesssim 0.01$, that is still within statistical uncertainty.

4 CONCLUSION AND DISCUSSION

In this paper, we reported the results of the continuum spectrum analysis about MAXI J1348-630 with an energy range 2–20 keV based on Insight-HXMT observations during the 2019 outburst. As the fiducial value of the input parameters, the distance of the source $D = 3.39 \text{kpc}$, the mass of the black hole $M = 11 M_{\odot}$ and the inclination of the system $i = 29.2^{\circ}$, the average spin of the black hole is determined as 0.41 ± 0.03 from the observation data in very soft state modeled by kerrbb, with the inner disk temperature at $0.47 \pm 0.01 \text{keV}$ and the apparent inner disk radius at $5.33 \pm 0.10 R_g$. Furthermore, due to the quite uncertainty of the input parameters D , M , i , we tested

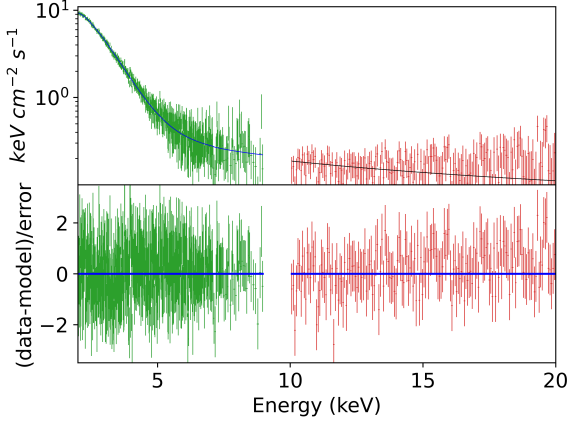


Figure 6. The spectrum and the residual for ObsID 403 with model 2 as an example. The green and red data points correspond to LE telescope and ME telescope, respectively.

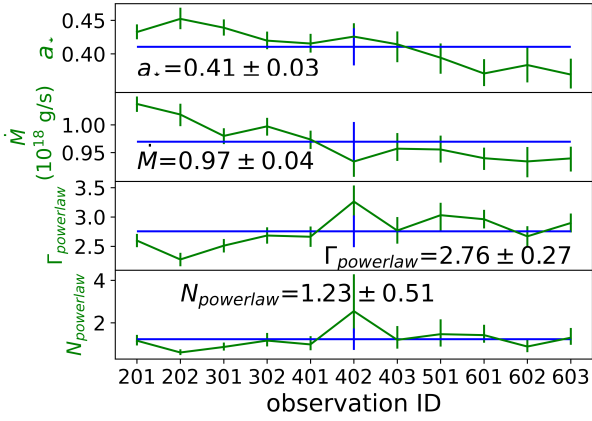


Figure 7. The fitted parameters versus the observation ID with model 2. a_* is the spin of black hole, \dot{M} for the effective mass accretion rate in units of 10^{18} g/s, $\Gamma_{powerlaw}$ for the photon index in powerlaw model, $N_{powerlaw}$ for the normalization of powerlaw model. The average results are shown in black font.

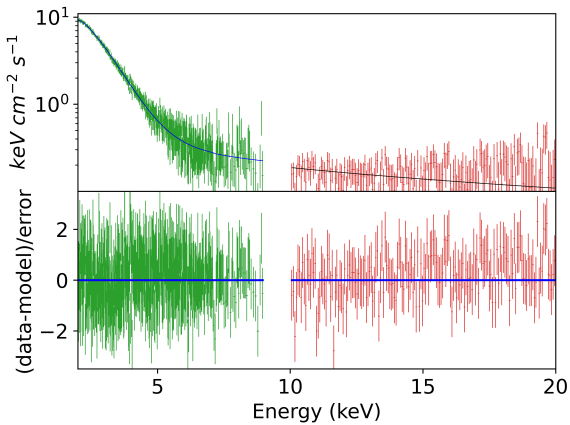


Figure 8. The spectrum and the residual for ObsID 403 with model 3 as an example. The green and red data points correspond to LE telescope and ME telescope, respectively.

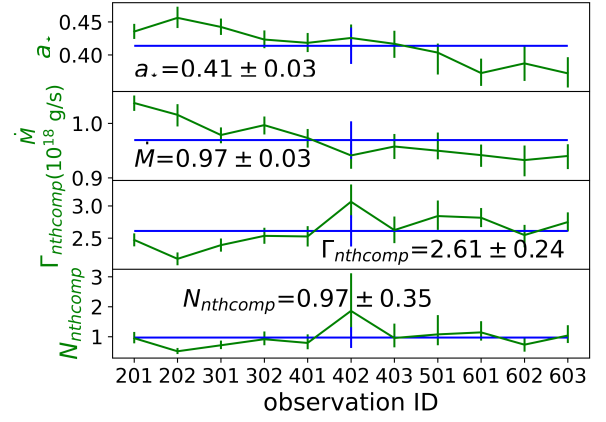


Figure 9. The fitted parameters versus the observation ID with model 3. a_* is the spin of the black hole, \dot{M} for the effective mass accretion rate in units of 10^{18} g/s, $\Gamma_{nthcomp}$ for the photon index in nthcomp model, $N_{nthcomp}$ for the normalization of nthcomp model. The average results are shown in black font.

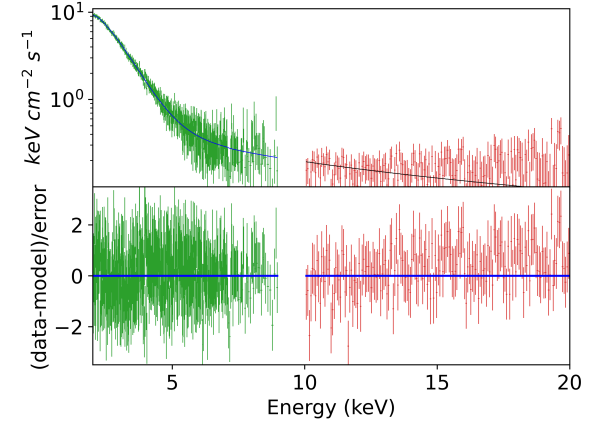


Figure 10. The spectrum and the residual for ObsID 403 with model 4 as an example. The green and red data points correspond to LE telescope and ME telescope, respectively.

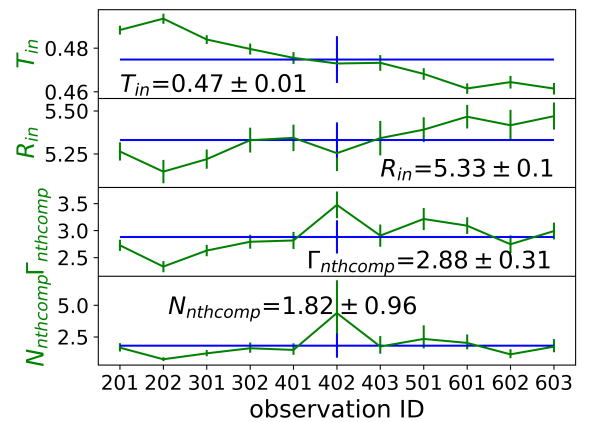


Figure 11. The fitted parameters versus the observation ID with model 4. T_{in} is the inner disc temperature, R_{in} for the apparent inner disc radius in units of R_g , $\Gamma_{nthcomp}$ for the photon index in nthcomp model, $N_{nthcomp}$ for the normalization of nthcomp model. The average results are shown in black font.

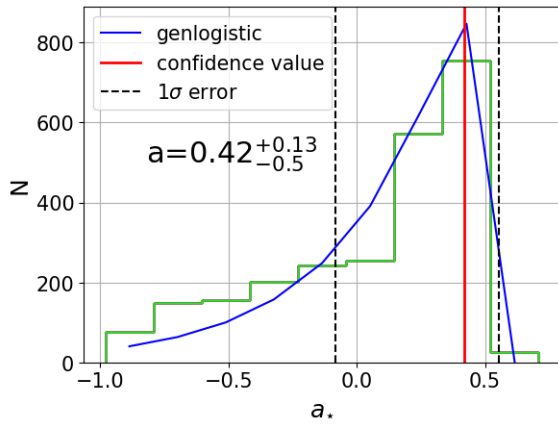


Figure 12. The distribution of a_* from the Monte Carlo method. The black dash lines illustrate 1σ error, the red line for the best-fitting value, and the blue line for the genlogistic distribution fitting.

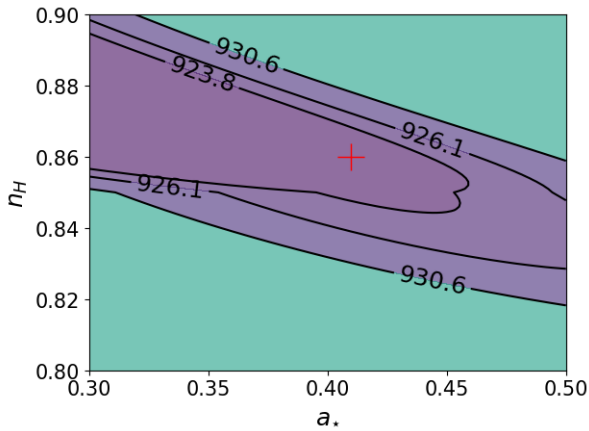


Figure 13. This contour figure is shown for iterating over N_H in the range of $(0.8 - 0.9) \times 10^{21} \text{ cm}^{-2}$ and a_* from 0.3 to 0.5. The red cross represents the best fit with $\chi^2 \sim 921.6$, the black line $\chi^2 \sim 923.8$ for 1σ , the black line $\chi^2 \sim 926.1$ for 2σ , the black line $\chi^2 \sim 930.6$ for 3σ .

the influence of these three parameters with Monte Carlo methods by setting over 2000 set parameters, e.g., $D : 1.6 - 4 \text{ kpc}$, $M : 8 - 13 M_\odot$, and $i : 25^\circ - 46^\circ$ so that the best-fitted distribution showed in Fig. 3.3 still confirms a moderate spin black hole of $a_* = 0.42^{+0.13}_{-0.50}$ (1σ error) in MAXI J1348-630.

For the test, we use the convolution model *simpl* to replace the *powerlaw* model to make the continuum fittings. The fitting results for ObsID 403 are $a_* \sim 0.41 \pm 0.01$, $\dot{M} \sim 0.97 \pm 0.01$, $\Gamma \sim 2.6^{+0.2}_{-1.9}$, hardening factor $\sim 0.016 \pm 0.003$, which is consistent with those of Model 2. Because the difference between the convolution model *simpl* and additive model *powerlaw* would concentrate on the bands below $\sim 2 \text{ keV}$ (Steiner et al. 2009), our data only covering from 2 - 20 keV will not be affected. In addition, we also tested the convolution model *thcomp* replacing *nthcomp* model in the fittings and got similar results.

In the continuum spectral fittings, we have taken four models to check the influence of the disc and non-thermal models (also see Fig. 14). From the comparison between model 2 and model 3, the influence of different non-thermal components could be ignored, and $a_* = 0.41 \pm 0.03$ from *kerrbb* also agreed with the results of the a_* distribution $0.42^{+0.13}_{-0.50}$ in section 3.3. From the fitting results of model

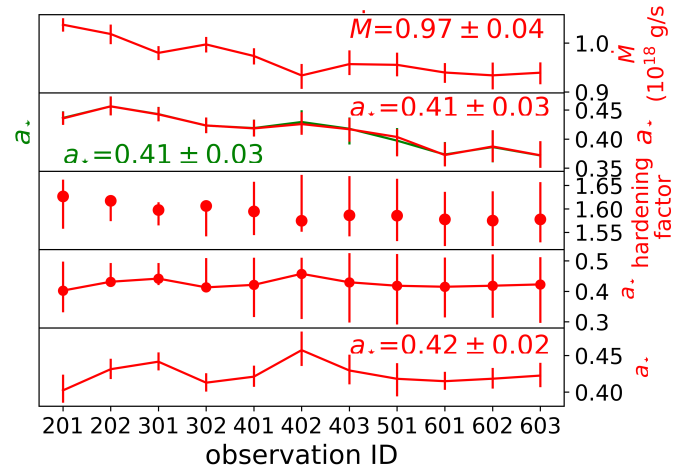


Figure 14. Comparison of the fitted parameters for two different models: 2 and 3. In the top panel: the red line is for the effective accretion rate \dot{M} in units of 10^{18} g/s . In the second panel: the green line is for a_* in model 2, and the red line is for a_* in model 3. In the third panel: in the spectral fittings, we allow the hardening factor to vary with the effective accretion rate \dot{M} , which declines with the declining luminosity and the mean hardening factor is found to be 1.59 and the error bars are given by iterating over hardening factor and a_* with 1σ . In the fourth panel: The spin parameter a_* is determined when the hardening factor changes as in the third panel and the error bars are given by iterating over hardening factor and a_* with 1σ . Since a_* and the hardening factor degenerate strongly and the error bars are large in the third and fourth panels. In the bottom panel: We fix the hardening factor at the center value of the traversal results, the spin parameter a_* with small error bars is illustrated in this panel. The BH spin does not show any significant evolution with the accretion rate with the mean value of $a_* \sim 0.42 \pm 0.02$.

1 and model 4, there is also little influence on the disk component from the non-thermal components. The *dikkbb* model gets consistent results: the mean apparent inner disk radius $R_{in} \sim 5.33 \pm 0.10 R_g$, and the inner disk temperature $T_{in} \sim 0.47 \pm 0.01 \text{ keV}$.

We noticed that the measured spin of the black hole declines over time slightly, $a_* \sim 0.45$ to ~ 0.37 . In the former 8 observations, the change of a_* is not obvious, but in the last 3 observations, the spin a_* falls down below 0.4. In *kerrbb* model, the effective accretion rate \dot{M} and a_* are strongly related (the Pearson product-moment correlation coefficient is 0.73), suggesting the trend of an apparently declining spin with declining luminosity or accretion rate. Since the spectral hardening can change with the luminosity (Davis et al. 2006), and we have fixed the hardening factor to be 1.6 in the previous fittings, so we here let the hardening factor be a free parameter and then study the effect on the measured values of a_* . We make the spectral fittings again with the hardening factor varying from 1.5 to 1.7 and the spin a_* from 0.3 to 0.5 in all the observations. In the third panel of Fig. 14, the hardening factor change from 1.62 to 1.58 with the declining luminosity, and then in the same time, the derived a_* does not show the declining trend with the observations, which is illustrated in the two bottom panels of Fig. 14.

ACKNOWLEDGEMENTS

We are grateful to the referee for the useful comments and suggestions. This work is supported by the National Key Research and Development Program of China (Grants No. 2021YFA0718503), the NSFC (12133007, U1838103). This work has made use of data

from the *Insight*-HXMT mission, a project funded by China National Space Administration (CNSA) and the Chinese Academy of Sciences (CAS).

DATA AVAILABILITY

Data that were used in this paper are from Institute of High Energy Physics Chinese Academy of Sciences (IHEP-CAS) and are publicly available for download from the *Insight*-HXMT website. To process and fit the spectrum, this research has made use of XRONOS and FTOOLS provided by NASA.

REFERENCES

- Alabarta K., Méndez M., García F., Peirano V., Altamirano D., Zhang L., Karpouzas K., 2022, *Monthly Notices of the Royal Astronomical Society* Bardeen J. M., Press W. H., Teukolsky S. A., 1972, *The Astrophysical Journal*, 178, 347
- Belloni T. M., Zhang L., Kylafis N. D., Reig P., Altamirano D., 2020, *Monthly Notices of the Royal Astronomical Society*, 496, 4366
- Bhowmick R., Debnath D., Jana A., Chatterjee D., Chatterjee K., Nath S. K., 2022, 44th COSPAR Scientific Assembly. Held 16-24 July, 44, 2256
- Blandford R., Payne D., 1982, *Monthly Notices of the Royal Astronomical Society*, 199, 883
- Blandford R. D., Znajek R. L., 1977, *Monthly Notices of the Royal Astronomical Society*, 179, 433
- Cangemi F., Rodriguez J., Belloni T., Gouiffès C., Grinberg V., Laurent P., Petrucci P.-O., Wilms J., 2022, arXiv preprint arXiv:2210.08561
- Cao X., et al., 2020, *SCIENCE CHINA Physics, Mechanics & Astronomy*, 63, 1
- Carotenuto F., Tremou E., Corbel S., Fender R., Woudt P., Miller-Jones J., 2019, *The Astronomer's Telegram*, 12497, 1
- Carotenuto F., Tetarenko A., Corbel S., 2022a, *Monthly Notices of the Royal Astronomical Society*, 511, 4826
- Carotenuto F., Corbel S., Tzioumis A., 2022b, *Monthly Notices of the Royal Astronomical Society: Letters*, 517, L21
- Chakraborty S., Ratheesh A., Bhattacharyya S., Tomsick J. A., Tombesi F., Fukumura K., Jaisawal G. K., 2021, *Monthly Notices of the Royal Astronomical Society*, 508, 475
- Chauhan J., et al., 2021, *Monthly Notices of the Royal Astronomical Society: Letters*, 501, L60
- Chen Y., et al., 2020, *Science China Physics, Mechanics & Astronomy*, 63, 1
- Cokelaer T., et al., 2022, cokelaer/fitter: v1.5.1, doi:10.5281/zenodo.7080297, <https://doi.org/10.5281/zenodo.7080297>
- Dabrowski Y., Fabian A., Iwasawa K., Lasenby A., Reynolds C., 1997, *Monthly Notices of the Royal Astronomical Society*, 288, L11
- Dauser T., García J., Parker M., Fabian A., Wilms J., 2014, *Monthly Notices of the Royal Astronomical Society: Letters*, 444, L100
- Davis S. W., Done C., Blaes O. M., 2006, *The Astrophysical Journal*, 647, 525
- Denisenko D., et al., 2019, *The Astronomer's Telegram*, 12430, 1
- Fabian A., Rees M., Stella L., White N. E., 1989, *Monthly Notices of the Royal Astronomical Society*, 238, 729
- García J. A., Dauser T., Steiner J. F., McClintock J. E., Keck M. L., Wilms J., 2015, *The Astrophysical Journal Letters*, 808, L37
- Guan J., et al., 2021, *Monthly Notices of the Royal Astronomical Society*, 504, 2168
- Jana A., Debnath D., Chatterjee D., Chakrabarti S. K., Chatterjee K., Bhowmick R., 2019, *The Astronomer's Telegram*, 12505, 1
- Jana A., Debnath D., Chatterjee D., Chatterjee K., Chakrabarti S. K., Naik S., Bhowmick R., Kumari N., 2020, *The Astrophysical Journal*, 897, 3
- Jia N., et al., 2022, *Monthly Notices of the Royal Astronomical Society*, 511, 3125
- Jithesh V., Misra R., Maqbool B., Mall G., 2021, *Monthly Notices of the Royal Astronomical Society*, 505, 713
- Kennea J., Negoro H., 2019, *The Astronomer's Telegram*, 12434, 1
- Kerr R. P., 1963, *Physical review letters*, 11, 237
- Kubota A., Tanaka Y., Makishima K., Ueda Y., Dotani T., Inoue H., Yamaoka K., 1998, *Publications of the Astronomical Society of Japan*, 50, 667
- Kulkarni A. K., et al., 2011, *Monthly Notices of the Royal Astronomical Society*, 414, 1183
- Kumar R., Bhattacharyya S., Bhatt N., Misra R., 2022, *Monthly Notices of the Royal Astronomical Society*, 513, 4869
- Lamer G., Schwobe A., Predehl P., Traulsen I., Wilms J., Freyberg M., 2021, *Astronomy & Astrophysics*, 647, A7
- Li L.-X., Zimmerman E. R., Narayan R., McClintock J. E., 2005, *The Astrophysical Journal Supplement Series*, 157, 335
- Li X., et al., 2023, arXiv preprint arXiv:2302.10714
- Liao J.-Y., et al., 2020, *Journal of High Energy Astrophysics*, 27, 24
- Liu C., et al., 2020, *SCIENCE CHINA Physics, Mechanics & Astronomy*, 63, 1
- Liu H., et al., 2022, *The Astrophysical Journal*, 938, 108
- Makishima K., Maejima Y., Mitsuda K., Bradt H., Remillard R., Tuohy I., Hoshi R., Nakagawa M., 1986, *The Astrophysical Journal*, 308, 635
- Mall G., Vadakkumthani J., Misra R., 2022, *Research in Astronomy and Astrophysics*
- Matsuoka M., et al., 2009, *Publications of the Astronomical Society of Japan*, 61, 999
- McClintock J. E., Shafee R., Narayan R., Remillard R. A., Davis S. W., Li L.-X., 2006, *The Astrophysical Journal*, 652, 518
- McClintock J. E., Narayan R., Steiner J. F., 2013, in *The Physics of Accretion onto Black Holes*. Springer, pp 295–322
- Misner C. W., Thorne K., Wheeler J., 1973, *San Francisco*, p. 660
- Mitsuda K., et al., 1984, *Publications of the Astronomical Society of Japan*, 36, 741
- Niedźwiecki A., Szanecki M., Zdziarski A. A., 2019, *Monthly Notices of the Royal Astronomical Society*, 485, 2942
- Novikov I. D., Thorne K. S., 1973, *Black Holes (Les Astres Occlus)*, pp 343–450
- Panizo-Espinar G., et al., 2022, arXiv preprint arXiv:2205.09128
- Penna R. F., McKinney J. C., Narayan R., Tchekhovskoy A., Shafee R., McClintock J. E., 2010, *Monthly Notices of the Royal Astronomical Society*, 408, 752
- Remillard R. A., McClintock J. E., 2006, *Annu. Rev. Astron. Astrophys.*, 44, 49
- Reynolds C. S., Nowak M. A., 2003, *Physics Reports*, 377, 389
- Russell T., Anderson G., Miller-Jones J., Degenaar N., Eijnden J. v., Sivakoff G. R., Tetarenko A., 2019, *The astronomer's telegram*, 12456, 1
- Saha D., Pal S., Mandal M., Manna A., 2021, arXiv preprint arXiv:2104.09926
- Sanna A., et al., 2019, *The astronomer's telegram*, 12447, 1
- Shafee R., McClintock J. E., Narayan R., Davis S. W., Li L.-X., Remillard R. A., 2005, *The Astrophysical Journal*, 636, L113
- Shafee R., McKinney J. C., Narayan R., Tchekhovskoy A., Gammie C. F., McClintock J. E., 2008, *The Astrophysical Journal*, 687, L25
- Shimura T., Takahara F., 1995, *The Astrophysical Journal*, 445, 780
- Steiner J. F., Narayan R., McClintock J. E., Ebisawa K., 2009, *Publications of the Astronomical Society of the Pacific*, 121, 1279
- Steiner J. F., McClintock J. E., Remillard R. A., Gou L., Yamada S., Narayan R., 2010, *The Astrophysical Journal Letters*, 718, L117
- Steiner J. F., et al., 2011, *Monthly Notices of the Royal Astronomical Society*, 416, 941
- Titarchuk L., Seifina E., 2022, arXiv preprint arXiv:2211.06271
- Tominaga M., et al., 2020, *The Astrophysical Journal Letters*, 899, L20
- Verner D., Ferland G. J., Korista K., Yakovlev D., 1996, arXiv preprint astro-ph/9601009
- Wang P., et al., 2022, *Monthly Notices of the Royal Astronomical Society*, 512, 4541
- Weng S.-S., Cai Z.-Y., Zhang S.-N., Zhang W., Chen Y.-P., Huang Y., Tao L., 2021, *The Astrophysical Journal Letters*, 915, L15
- Wilms J., Allen A., McCray R., 2000, *The Astrophysical Journal*, 542, 914
- Wu H., Wang W., Sai N., 2023, *Journal of High Energy Astrophysics*, 37, 25
- Yatabe F., et al., 2019, *The Astronomer's Telegram*, 12425, 1

- Zdziarski A. A., Johnson W. N., Magdziarz P., 1996, *Monthly Notices of the Royal Astronomical Society*, 283, 193
- Zdziarski A. A., Szanecki M., Poutanen J., Gierliński M., Biernacki P., 2020, *Monthly Notices of the Royal Astronomical Society*, 492, 5234
- Zdziarski A. A., You B., Szanecki M., Li X.-B., Ge M., 2022, *The Astrophysical Journal*, 928, 11
- Zhang S. N., Cui W., Chen W., 1997, *The Astrophysical Journal*, 482, L155
- Zhang S.-N., et al., 2020a, *Science China Physics, Mechanics & Astronomy*, 63, 1
- Zhang L., et al., 2020b, *Monthly Notices of the Royal Astronomical Society*, 499, 851
- Zhang W., et al., 2022, *The Astrophysical Journal*, 927, 210
- Zhao X.-S., et al., 2020, *Journal of High Energy Astrophysics*, 27, 53
- Zhao X., et al., 2021, *The Astrophysical Journal*, 916, 108

This paper has been typeset from a \TeX/L\AA\TeX file prepared by the author.